Revision 1

Revised mineral and Mg# maps of the Moon from integrating results from the Lunar Prospector neutron and gamma ray spectrometers with Clementine spectroscopy

Sarah T. Crites[1,*] and Paul G. Lucey[1]

[1] Hawai'i Institute of Geophysics and Planetology, University of Hawai'i at Manoa, 1680 East West Rd POST 602, Honolulu, HI 96822, USA

*Corresponding author. Tel: +1-808-956-6488. Fax: +1-808-956-3188. Email: scrites@higp.hawaii.edu

ABSTRACT

Mineralogical measurements from spectral remote sensing and remote geochemical measurements from gamma ray and neutron spectrometers are complementary datasets that have been used together successfully to study the distributions of iron, titanium, and rare earth elements on the Moon. We compare neutron and gamma ray datasets from Lunar Prospector and find them in good agreement with each other within the errors of previously developed equations that relate neutron flux with geochemistry, but find small adjustments to the nominal values are warranted. We used the neutron-validated LP GRS oxides to improve Clementine-based global mineral maps. The comparison was enabled by converting the minerals of Lucey (2004) to oxides using stoichiometry and assumptions about Mg#, calcium content of clinopyroxenes, and An#. We find that FeO and Al_2O_3 derived from the maps of Lucey (2004) do not follow the expected negative correlation seen in lunar samples, but can be brought into agreement with samples and with LP GRS oxides by increasing plagioclase in proportion with orthopyroxene

abundance, while simultaneously decreasing Mg#. We interpreted this to mean that plagioclase and orthopyroxene exist in rocks together (as in a noritic rock) with the spectrally difficult to detect plagioclase being masked by the strong spectral signature of the orthopyroxene. We generated a revised set of maps of the major lunar minerals and a map of Mg# for the mafic minerals that are consistent with Lunar Prospector neutron and gamma ray spectrometer results and show greatly improved agreement with lunar soil samples over previous global mineral maps from Clementine.

Keywords: remote sensing; mineralogy; lunar magma ocean; neutron spectroscopy; gamma ray spectroscopy; visible spectroscopy

INTRODUCTION

Visible and near-infrared spectroscopy of the Moon provides a tool that is sensitive to both the major minerals and chemistry of the lunar surface. Minerals detected through spectroscopy help constrain their spatial distribution and the distribution of interpreted rock types that make up the Moon, with the high-calcium pyroxene-rich maria distinct from the plagioclase-rich highlands (e.g. McCord et al., 1981). Spectrally derived mineralogy can play an important role in deciphering the history and evolution of the Moon. For example, the "purest anorthosite" (PAN) detections of Ohtake et al. (2009) and Pieters et al. (2009) with <2 vol% mafic minerals suggest that the lunar magma ocean may have concentrated plagioclase to a high degree in many locations across the Moon. Orbital neutron and gamma ray measurements (e.g., Feldman et al., 2000; Prettyman et al., 2006) provide geochemical measurements of the same geologic truth which, because of the Moon's comparatively simple mineralogy, can be compared with spectrally-derived mineralogy using relatively few assumptions to draw robust conclusions about lunar surface mineralogy.

Lucey (2004) produced global maps for the major lunar minerals olivine, orthopyroxene, clinopyroxene, and plagioclase from the Clementine mission's spectral reflectance measurements. However, these maps were not validated against other data sets or by comparison with lunar samples. The Lunar Prospector mission (Binder, 1998) followed Clementine with a gamma ray spectrometer (GRS) that directly measured elemental abundance (Prettyman et al., 2006) and a neutron spectrometer (NS) to provide a measurement of the weighted sum of the components present in the surface (e.g., Feldman et al., 2000). The Lunar Prospector measurements are independently sensitive to composition, so we perform a direct comparison, achieved through modeling and empirical relationships, to improve understanding of uncertainties in both measurements. We then compare the neutron-validated Lunar Prospector gamma ray measurements against mineral maps from spectral reflectance using simple stoichiometry. We use independent and complementary measurements by the Lunar Prospector gamma ray spectrometers to validate and improve the mineral maps, using lunar sample compositional trends as an additional constraint.

METHODS

Lunar prospector neutron and gamma ray spectrometer reconciliation

The Lunar Prospector mission carried a gamma ray spectrometer and a neutron spectrometer to study the composition of the lunar surface (Feldman et al., 1999). The gamma ray spectrometer measured gamma rays emitted from the lunar surface as a result of cosmic ray interaction with the major elements or radioactive decay of K, Th, and U. It also measured fast neutrons ($E > 500$ keV) using its anticoincidence shield (Feldman et al., 1999). The neutron spectrometer measured neutrons created as by-products of cosmic ray bombardment of the lunar surface and moderated to the thermal ($E < 0.4$ eV) and epithermal (0.4 eV $< E < 500$ keV)

energy ranges. The gamma ray dataset can be used to validate and improve spectral mineral maps, but for greater robustness we first examined the consistency of the gamma ray and neutron data with each other.

Fast neutron and gamma ray reconciliation. Gasnault et al. (2001) determined through modeling of neutron production, transport, and leakage, as well as comparisons to laboratory experiments, a linear relationship between fast neutron leakage counts per unit time and the average atomic mass of the constituents of the material producing neutrons. This equation is given by (1) (Gasnault et al., 2001), where $\langle A \rangle$ is the average atomic mass in units of amu (atomic mass units), and C is the fast neutron leakage in counts per unit time (neutrons per second).

$$\langle A \rangle = eC + f$$

$$e = (26 \pm 6) \times 10^{-3}$$

$$f = (11 \pm 3)$$

Fast neutron count rates can be estimated using the oxides measured by the LP GRS and equation 1. This can then be compared with the measured fast neutron count rate. We compared the distribution of fast neutron count rates for the Moon, calculated from LP GRS average atomic mass, and measured fast neutron count rate, both binned to 2 degree pixels, shown in Figure 1a. The distribution falls off the plotted 1:1 line, with the measured fast neutron count rate systematically higher than that estimated from the gamma ray spectrometer data and equation 1. We applied a simple adjustment of the parameters e and f within their stated errors to minimize the differences between the two datasets and this resulted in an improved fit (Fig. 1b) when $e = 25.6 * 10^{-3}$ and $f = 10.6$.

Epithermal and thermal neutron and gamma ray reconciliation. The ability of a material to absorb thermal neutrons is called the macroscopic neutron absorption cross section and is a weighted sum of the thermal neutron absorption cross sections of the constituent elements:

$$\Sigma_{eff} = \sum_i \frac{\sigma_i f_i N_A}{A_i}$$

where σ_i is the thermal neutron absorption cross section of constituent i, f_i is the weight fraction of i, A_i is the atomic mass of i, and N_A is Avogadro's number (Elphic et al., 2000). All components of the medium contribute to the macroscopic neutron absorption cross section, but those with relatively large cross sections that are present in significant quantities like iron and titanium, have a particularly large effect on the total cross section. In addition, some isotopes of samarium and gadolinium, though they are present in lunar soil only at the ppm level, have a large contribution to the total cross section because their thermal neutron absorption cross sections are orders of magnitude larger than those of the other constituent elements of lunar soil (Elphic et al., 2000). Table 1 gives the thermal neutron cross sections for the major elements as well as the important rare earth elements Sm and Gd. The abundances of Sm and Gd were not measured directly using gamma ray spectroscopy, but they are correlated with each other and with thorium in lunar samples (e.g., Jolliff, 1998; Korotev, 2000) so they can be inferred if assumptions are made about the Sm/Th ratio and the Gd/Sm ratio and the distribution of isotopes.

106 The count rates of thermal and epithermal neutrons from the lunar surface can be related
107 to the macroscopic neutron absorption cross-section of the surface being treated by neutron
108 transport models for the lunar samples (Feldman et al., 2000). Elphic et al. (2000) used a linear
109 approximation for the relationship between macroscopic neutron absorption cross section and the
110 epithermal to thermal neutron ratio given by (3), where f_{epi} and f_{thermal} are the measured
111 epithermal and thermal neutron count rates, respectively.

$$\Sigma_{eff} = a * \left({f_{epi}}/{f_{thermal}} \right) - b$$

$$a = 5.252 \times 10^{-3}$$

112 $$b = 1.485 \times 10^{-3}$$

113 The elements measured by the LP GRS can be compared with thermal and epithermal
114 neutron data using equations 2 and 3 along with assumptions about Sm/Th and Gd/Sm ratios for
115 the lunar surface using the microscopic neutron absorption cross sections of the elements. We
116 assumed Gd=1.17*Sm (Jolliff, 1998; Korotev, 2000) and, following Gillis et al. (2003) used a
117 beginning assumption of Sm=2.7*Th. The result of a comparison using these assumptions and
118 equations 2 and 3 are shown in Figure 2a. This distribution also falls systematically off the 1:1
119 correlation line. We performed an optimization varying the parameters of equation 3 within 2σ
120 and allowing the Sm/Th ratio, which has a wide range in lunar samples (Wieczorek et al., 2006),
121 to vary. The two datasets were brought into agreement with minor modifications of the
122 parameters of equation 3 to $a = 5.732 * 10^{-3}$ and $b = 1.386 * 10^{-3}$ and a global Sm/Th ratio of
123 2.39. Table 2 summarizes the modified parameters for equations 1 and 2 resulting from our
124 neutron and gamma ray reconciliation.

Reconciliation of Clementine-based mineral maps with Lunar Prospector

Mineral-map derived oxides and GRS. The Clementine mission mapped the Moon in 11 multispectral bands at 100-200 m spatial resolution from ultraviolet to near-infrared wavelengths (Nozette et al., 1994). Lucey (2004) used radiative transfer modeling to match computed spectra of mixtures of the major lunar minerals olivine, plagioclase, orthopyroxene, and clinopyroxene with observed Clementine spectra of the lunar surface. Because the exposure of the lunar surface to space weathering results in decreased spectral contrast, the optical maturity parameter of Lucey et al. (2000a, 2000b) was used to limit the analysis to fresh exposures (optical maturity > 0.3). Fresh exposures identified in this way made up 2.3% of the lunar surface, and the mineral maps were interpolated to fill the gaps between them. The result was global mineral maps for olivine, plagioclase, orthopyroxene, clinopyroxene, and mafic mineral magnesium number (Mg#, assumed to be the same for all mafic minerals) of varying spatial resolution in the final dataset (Lucey, 2004) which we used in this analysis.

The mineral maps can be converted to oxides for direct comparison to the LP GRS oxides using simple stoichiometry along with assumptions about Mg# for olivine and pyroxene and calcium content for clinopyroxene. Using the Mg# map produced by Lucey (2004) as the Mg# for the mafic minerals, and assuming Wo_{40} for clinopyroxene (Papike et al., 1998) we produced global maps of SiO_2, Al_2O_3, FeO, MgO, and CaO. The abundance of ilmenite was inferred from the TiO_2 abundances of Gillis et al. (2003) and then converted back into TiO_2 and FeO to complete mapping of the major oxides measured by the LP GRS. The mineral map-derived oxides were then sampled at the 2 °/pixel resolution of the LP GRS oxides. Figure 3a-f shows the correlation between LP GRS oxides and mineral map-derived oxides. There is significant scatter for all of the oxides except iron, for which good agreement is expected because the LP

148 GRS FeO distribution was a constraint in the construction of the mineral maps (Lucey, 2004).
149 For the rest of the oxides either poor correlation is present, or the signal to noise ratio in the data
150 sets relative to the variation in the element may obscure a correlation. The relationship between
151 the mineral map and LP GRS aluminum is strikingly non-linear and especially merited further
152 investigation.

153 Al_2O_3 and FeO show a strong negative correlation in lunar samples (e.g., Haskin and
154 Warren, 1991; Korotev et al., 2003). Prettyman et al. (2006) used lunar sample and meteorite
155 data to obtain the relationship $Al_2O_3 = -1.2\ FeO + 32.4$, $R^2=0.95$ and used this trend to adjust the
156 calibration of the LP GRS iron and aluminum data. The resulting trend, shown in Figure 4a,
157 contrasts vividly with the nonlinear relationship between FeO and Al_2O_3 obtained from the
158 mineral maps of Lucey (2004), shown in Figure 4b. Investigation of the spatial distribution of
159 the low-iron, low-aluminum region of Figure 4b-revealed a correspondence with high
160 orthopyroxene detections presented by Lucey (2004) (Figure 5a,b). The detection of
161 orthopyroxene is robust as this mineral is the most distinct of the lunar minerals (Lucey 2004).
162 However, plagioclase is featureless across the region used by Lucey (2004), and easily masked
163 by the presence of other minerals. If orthopyroxene were correlated with plagioclase (as in a
164 noritic rock), the plagioclase might be obscured. We postulated that orthopyroxene detections
165 may in fact be rocks of mixed orthopyroxene and plagioclase composition.

166 Following this hypothesis, we performed an optimization in which we added plagioclase
167 in proportion with orthopyroxene, renormalizing the minerals to 100% with each step. The
168 metric for improvement was the linear correlation coefficient between FeO and Al_2O_3 from the
169 modified mineral maps. In order to maintain agreement of the new mineral maps with LP GRS
170 iron, it was necessary to decrease Mg# for the mafic minerals for the same pixels, in proportion

with orthopyroxene abundance. We constrained the iron abundance calculated from the modified mineral maps to maintain a linear correlation coefficient of 0.73 or better with the LP GRS FeO, with the mean of the modified mineral map FeO constrained to remain within 0.55 wt.% of the LP GRS FeO. Figure 6 shows the result of this optimization, with the modified mineral maps showing improved agreement with the iron-aluminum trend seen in lunar samples. Figure 7 shows a comparison of the major oxides calculated from the optimized mineral maps compared with the LP GRS oxides. The non-linear behavior of the mineral map-derived aluminum was eliminated, and as a secondary result of improving the iron-aluminum trend by decreasing the Mg# for the mafic minerals, mineral map MgO was also brought into better agreement with the LP GRS oxide.

Revised mineral map Mg#. Lucey (2004) modeled mafic mineral chemistry in the form of the magnesium number (Mg# = mole percent MgO/(MgO+FeO)) in order to obtain maps of the major lunar minerals. We used this original Mg# map (Fig. 8a; not explicitly reported in Lucey (2004)) as a starting point for our optimization. After decreasing Mg# relative to orthopyroxene to maintain agreement of our new, higher plagioclase mineral maps with LP GRS iron, we obtained the optimized Mg# map of Figure 8b. Prettyman et al. (2006) commented on the difficulty of measuring variations in Mg# with the LP GRS data because of the low precision of the MgO data. Despite this caution, the Mg# values seen in our optimized map ranged from about 40 to 80, generally consistent with the range seen by the LP GRS.

However, the revised Mg# map strongly differs from the Mg# from LP GRS (Fig. 6c) in the western maria (outlined in black). The western maria are unique: they are among the youngest mare basalts on the surface of the Moon (e.g. Heisinger and Head, 2011); they have relatively high TiO_2 (~2-9 vol.%, e.g., Pieters, 1978; Elphic et al., 2002; Prettyman et al., 2006);

194 they are high in iron (~15-25 vol.%, e.g., Lucey et al., 2000a; Staid and Pieters, 2001; Elphic et
195 al., 2002; Lawrence et al., 2002; Prettyman et al., 2006); and they have been mapped as olivine-
196 rich on the basis of an unusually strong 1 μm absorption combined with weak absorption at 2 μm
197 by many authors (e.g., Pieters et al., 1980; Staid and Pieters, 2001; Lucey, 2004; Staid et al.,
198 2011), as well as by this study (Figure 11c). Staid et al. (2011) concluded on the basis of
199 stratigraphic studies and the iron-rich composition of these olivine-rich basalts likely originated
200 from residual melts, possibly in a mantle magma chamber undergoing mineral fractionation and
201 settling. If the olivines in this unique region are of a separate origin than the other minerals, it
202 would be reasonable to decouple the Mg# for olivine from that of the other minerals.

203 To bring our Mg# map into better agreement with Lunar Prospector in this region, we
204 decreased Mg# for olivine only in the outlined region of the western maria, maintaining the Mg#
205 for orthopyroxene and clinopyroxene at the values seen in Figure 8b, until the mean of the Mg#
206 calculated from the mineral-map derived oxides in that region equaled the mean of the LP GRS
207 Mg# in the same region. An Mg# of 24.3 for olivine in this region was required to reach a mean
208 value equal to the GRS mean Mg# of 39.4. This calculation takes the published LP GRS oxides
209 at face value; however, Prettyman et al. (2006) observed that in the western Procellarum region,
210 the sum of all six LP GRS oxides (expected to be 100% in the absence of systematic errors)
211 shows a deficit of about 6%. This could be the result of 1% error in each of the six oxides, or an
212 underestimate of 6% in one of the oxides (Prettyman et al., 2006). Taking the extreme case, if
213 we assume MgO is the underestimated oxide and increase its abundance by 6% in the western
214 Procellarum region, the average Mg# of this region increases from 39.4 to 53.5. An Mg# of 53.6
215 for olivine would then be sufficient to bring the average Mg# in this region into agreement with
216 the modified LP GRS Mg#. However, since it is unknown to which oxide this error should be

assigned, our final Mg# map is the one derived from our minerals maps with modified olivine Mg# in agreement with the published LP GRS oxides, and is shown in Figure 8d. While the overall mean of the LP GRS Mg# is still higher than the mean of our final Mg# map (62 vs. 57), our maps cover the same Mg# range and fall much closer to the LP GRS values than the original Mg# map of Lucey (2004), which had a mean Mg# of 78.

The effect of lowering the overall Mg# in this region was an upturn in FeO abundances above the LP GRS trend for this region (Figure 9a). To counter this effect we increased plagioclase in this region, renormalizing the minerals to 100% with each step, until the mean FeO content derived from the mineral maps was equal to the mean FeO from LP GRS. The result of this adjustment, which required a 7 vol.% increase in plagioclase on average (after renormalization to 100%), is shown in Figure 9b. Figure 9c shows the aluminum-iron trend that results after adjusting Mg# and plagioclase content. Our final adjustments resulted in a distinct break in the slope of the aluminum-iron trend. However, some non-linearity is also seen in lunar sample data as a result of soils that are not simple mixtures of mare basalt and feldspathic highland soil as well as the higher FeO/MgO ratio of mare basalts relative to highland samples (Fischer and Pieters, 1995; Lucey et al., 2006). A comparison of FeO+MgO with Al_2O_3 removed nonlinear effects introduced by varying FeO/MgO ratios and revealed general good agreement with the linear trend seen in lunar samples (solid line; Lucey et al., 2006).

Ohtake et al. (2012) reported an Mg# map for the lunar highlands obtained using spectra from the Kaguya Spectral Profiler (Fig. 10b). A comparison of our optimized Mg# map with the map of Ohtake et al. (2012) reveals qualitative spatial agreement between the two maps, with Mg# highest in the farside highlands, and similar mean values (56 from the map of Ohtake et al. (2012), 61 from our optimized map).

RESULTS AND DISCUSSION

The result of this study is a new set of global major mineral maps, based on Clementine UVVIS spectra, validated and improved by comparison with global data from Lunar Prospector's neutron and gamma ray spectrometers. The Lunar Prospector-validated maps of plagioclase, clinopyroxene, orthopyroxene, olivine, and ilmenite are shown in Figure 11.

The new maps are generally similar to the maps of Lucey (2004) with some striking differences. The average plagioclase content of the highlands in the new maps is over 80 vol.%, in contrast with an average of 75 vol.% in the 2004 maps. Plagioclase remains anti-correlated with clinopyroxene as in the maps of Lucey (2004), reflecting mare-highland differences. Our comparison of mineral-map derived oxides with GRS oxides revealed that plagioclase, easily masked spectrally by the strong orthopyroxene signature, is likely to coexist with orthopyroxene across the lunar surface, as in noritic materials, so in our revision of the mineral maps we have introduced a correlation of plagioclase with orthopyroxene that is visible in the maps.

Clinopyroxene is the dominant mafic mineral in the maria with the exception of the anomalous western maria, where olivine reaches equal proportions. Clinopyroxene is also present at a relatively high level throughout the highlands and accounts for about 50% of the total mafic contribution to the highlands. This is consistent with the detection of high-calcium pyroxene in fresh craters with diameters between 8 and 24 km throughout the lunar highlands by Ogawa et al. (2011) using Kaguya Spectral Profiler data.

The mean of the revised olivine distribution is slightly lower than that estimated by Lucey (2004), near 7 vol.% rather than 10 vol.%, but some areas of the western maria maintain olivine contents as high as 30-40 vol.%. The revised distribution of orthopyroxene is similar to

262 that in the maps of Lucey (2004), with average contents slightly lower (5 vol.% rather than 10
263 vol.%). The distribution of ilmenite is almost entirely dependent on the TiO_2 maps of Gillis et al.
264 (2003) and was changed very little by the optimization.

265 Throughout this study we used major-element relationships from lunar samples and
266 gamma ray spectroscopy to improve our spectroscopy-based mineral maps; lunar sample
267 mineralogy provides another point of reference for our revised mineral abundances. In the
268 proceedings of the first Conference on the Lunar Highlands Crust Stöffler et al. (1980) proposed
269 a classification scheme for lunar highland rocks based in part on their positions in compositional
270 fields on plagioclase-pyroxene-olivine and plagioclase-orthopyroxene-clinopyroxene ternary
271 diagrams. Although the rock type compositional fields were intended only for the classification
272 of plutonic lunar highland rocks (Stöffler et al., 1980), since the Moon's major mineralogy is
273 largely restricted to plagioclase, olivine, and pyroxene (e.g., Papike et al., 1998), these ternary
274 diagrams provide a useful way to visualize mineralogy of samples and remote sensing data from
275 all areas of the Moon including the maria.

276 The mineral distribution of the Lucey (2004) maps on the plag-pxn-ol ternary of Figure
277 12a includes a field of points that fall outside the outlined field in which the known lunar soils
278 from the Apollo and Luna missions and the feldspathic lunar meteorites plot. Figure 12b shows
279 the dramatically improved agreement of the Lunar Prospector-validated mineral maps of this
280 study with the field occupied by lunar samples. Figure 12c shows the distribution in mineralogy
281 of the revised maps on the plag-opx-cpx ternary used by Stöffler et al. (1980) for classification of
282 highland rocks, and highlights the presence of clinopyroxene as a major mafic mineral for much
283 of the lunar surface. Mare-highland differences are reflected in Figure 12c, in which
284 clinopyroxene is highest where plagioclase is low.

IMPLICATIONS

We derived a robust set of global mineral maps based on Clementine UVVIS spectroscopy and validated against the self-consistent Lunar Prospector gamma ray and neutron spectrometer datasets. The revised mineral maps are in good agreement with lunar sample mineralogy. The distribution of highlands Mg# measurements in the revised maps are consistent with the Mg# measurements of Ohtake et al. (2012). The plagioclase content of these Lunar Prospector-validated maps is significantly higher than that of the original global mineral maps of Lucey (2004) and shows a pronounced plagioclase high in the central farside highlands that may be the remnant of an anorthositic craton (Jolliff et al. 2000). The revised mineral maps provide a tool that can be used for the examination of hypotheses of lunar formation and evolution and demonstrate the usefulness of LP gamma ray data as a validation tool for spectral mineral maps and algorithms.

Our maps agree with the widespread detections of high-Ca pyroxene in the lunar highlands by Ogawa et al. (2011). Ogawa et al. (2011) suggested this could indicate the presence of a deep gabbroic layer beneath the anorthositic crust or abundant calcium-rich trapped liquid. The work of Lucey et al. (this volume) did not detect comparable high-Ca pyroxene abundances in small (<1 km diameter) fresh craters indicating the small crater results may be sampling a different crustal layer than the 8-24 km craters studied by Ogawa et al. (2011). Craters of the size range studied by Lucey et al. (this volume) make up only a small percentage of the immature surfaces the mineral maps of this work were based on, so the contrast between the small crater mineralogy of Lucey et al. (this volume) and our results may indicate that the two studies are sampling different crustal layers. These studies and that of Ogawa et al. (2011)

highlight the fact that the origin and vertical distribution of high-Ca pyroxene in the lunar highlands remains unexplained and is an important topic for future investigation.

REFERENCES CITED

Binder, A.B. (1998) Lunar Prospector: Overview. Science, 281, 1475-1476.

Elphic, R. C., Lawrence, D.J., Feldman, W.C., Barraclough, B.L., Maurice, S., Binder, A.B., and Lucey, P.G. (2000) Determination of lunar global rare earth element abundances using Lunar Prospector neutron spectrometer observations. Journal of Geophysical Research, 105, E8, 20,333– 20,346.

Elphic, R. C., Lawrence, D.J., Feldman, W.C., Barraclough, B.L., Gasnault, O.M., Maurice, S., Lucey, P.G., Blewett, D.T., and Binder, A.B. (2002) Lunar Prospector neutron spectrometer constraints on TiO_2. Journal of Geophysical Research, 107, E4, 5024,8-1—8-8.

Feldman, W.C., Barraclough, B.L., Fuller, K.R., Lawrence, D.J., Maurice, S., Miller, M.C., Prettyman, T.H., and Binder, A.B. (1999) The Lunar Prospector gamma ray and neutron spectrometers. Nuclear Instruments and Methods in Physics Research A, 422, 562-566.

Feldman, W. C., Lawrence, D.J., Elphic, R.C., Vaniman, D.T., Thomsen, D.R., Barraclough, B.L., Maurice, S., and Binder, A.B. (2000) The chemical information content of lunar thermal and epithermal neutrons. Journal of Geophysical Research, 105, E8, 20,347– 20,364.

Fischer, E.M. and Pieters, C.M. (1995) Lunar surface aluminum and iron concentration from Galilio solid state imaging data, and the mixing of mare and highland materials. Journal of Geophysical Research, 100, 23279-23290.

Gasnault, O., Feldman, W.C., Maurice, S., Genetay, I., d'Uston, C., Prettyman, T.H., and Moore, K.R., (2001) Composition from fast neutrons: application to the Moon. Geophysical Research Letters, 28, 19, 3797-3800.

Gillis, J.J., Jolliff, B.L., and Elphic, R.C. (2003) A revised algorithm for calculating TiO2 from Clementine UVVIS data: A synthesis of rock, soil, and remotely sensed TiO2 concentrations. Journal of Geophysical Research, 108, E2, 5009, doi: 10.1029/2001JE001515.

Haskin, L. and Warren, P. (1991) Lunar chemistry. In G.H. Heiken, D. T. Vaniman, and B. M. French, Eds., The Lunar Sourcebook, pp 357-449, Cambridge University Press, Cambridge.

Hiesinger, H., Head, J.W. III, Wolf, U., Jaumann, R., and Neukum, G. (2011) Ages and stratigraphy of lunar mare basalts: A synthesis. Special Papers of the Geological Society of America, 477 1-51, doi: 10.1130/2011/2477(01).

Jolliff, B.L. (1998) Large-scale separation of K-frac and REEP-frac in the source regions of Apollo impact-melt breccias, and a revised estimate of the KREEP composition. International Geology Review, 40, 916-935.

Jolliff, B.L., Gillis, J.J., Haskin, L.A., Korotev, R.L., and Wieczorek, M.A. (2000) Major lunar crustal terranes: Surface expressions and crust-mantle origins. Journal of Geophysical Research, 105, E5, 4197-4216.

Korotev, R.L. (2000) The great lunar hot spot and the composition and origin of the Apollo mafic ("LKFM") impact melt breccias. Journal of Geophysical Research, 105, 4317-4346.

Korotev, R.L., Jolliff, B.L., Ziegler, R.A., Gillis, J.J., and Hasken, L.A. (2003) Feldspathic lunar meteorites and their implications for compositional remote sensing of the lunar surface and the

348 composition of the lunar crust. Geochimica et Cosmochimica Acta, 107, 24,4895-24,4923,
349 doi:10.1016/j.gca.2003.08.001.

350 Lawrence, D.J., W.C. Feldman, R.C. Elphic, R.C. Little, T.H. Prettyman, S. Maurice, P.G.
351 Lucey, and A.B. Binder (2002) Iron abundances on the lunar surface as measured by the Lunar
352 Prospector gamma-ray and neutron spectrometers. Journal of Geophysical Research, 107, E12,
353 13-1—13-26, doi: 10.1029/2001JE001530.

354 Lucey, P.G., Blewett, D.T., and Jolliff, B.L. (2000a) Lunar iron and titanium abundance
355 algorithms based on final processing Clementing UVVIS images. Journal of Geophysical
356 Research, 105, E8, 20297-20305.

357 Lucey, P.G., Blewett, D.T., Taylor, G.J., and Hawke, B.R. (2000b) Imaging of lunar surface
358 maturity. Journal of Geophysical Research, 105, E8, 20,377-20,386.

359 Lucey, P.G. (2004) Mineral maps of the moon. Geophysical Research Letters, 31, L08701,
360 doi:10.1029/2003GL019406.

361 Lucey, P.G. et al. (2006) Understanding the lunar surface and space-Moon interactions. In Jolliff,
362 B.L., Wieczorek, M.A., Shearer, C.K., and Neal, C.R, Eds., New Views of the Moon, pp 83-219,
363 Mineralogical Society of America.

364 McCord, T.B., et al. (1981) Moon: Near-infrared spectral reflectance, a first good look. Journal
365 of Geophysical Research, 86,10,883-10,892.

366 National Nuclear Data Center, 2010. Evaluated Nuclear Data File (ENDF) Retrieval & Plotting <
367 http://www.nndc.bnl.gov/sigma/>.

Nozette, S., et al. (1994) The Clementine Mission to the Moon: Scientific Overview. Science, 266.5192, 1835-1839.

Ogawa, Y., et al. (2011) The widespread occurrence of high-calcium pyroxene in bright-ray craters on the Moon and implications for lunar-crust composition. Geophysical Research Letters, 38, L17202, doi: 10.1029/2011GL048569.

Ohtake, M. et al. (2009) The global distribution of pure anorthosite on the Moon. Nature, 461, 236-240.

Ohtake, M., et al. (2012) Primitive farside highland materials detected by Mg number. 43rd Lunar and Planetary Science Conference, Houston, TX, abstract # 1977.

Papike, J.J., Ryder, G., and Shearer, C.K. (1998) Lunar Samples. In Papike, J.J. Ed., Planetary Materials, Reviews in Mineralogy 36, pp 5-1-5-234, Mineralogical Society of America.

Pieters, C.M. (1978) Mare basalt types on the front side of the Moon. Proceedings of the 9th Lunar and Planetary Science Conference, p. 2825-2849.

Pieters, C.M., Head, J.W., Adams, J.B., McCord, T.B., Zisk, S.H., and Whitford-Stark, J.L. (1980) Late high-titanium basalts of the western maria: Geology of the Flamsteed region of Oceanus Procellarum. Journal of Geophysical Research, 85, 3913-3938, doi: 10.1029/JB085iB07p03913.

Pieters, C.M. et al., (2009) Mineralogy of the lunar crust in spatial context: first results from the Moon Mineralogy Mapper (M^3). 40th Lunar and Planetary Science Conference, Houston, TX, Abstract #2052

Pieters, C.M., Stankevich, D.G., Shkuratov, Y.G., and Taylor, L.A. (2002) Statistical analysis of the links among lunar mare soil mineralogy, chemistry, and reflectance spectra. Icarus 155, 285-298.

Prettyman, T.H., Hagerty, J.J., Elphic, R.C., Feldman, W.C., Lawrence, D.J., McKinney, G.W., and Vaniman, D.T. (2006) Elemental composition of the lunar surface: Analysis of gamma ray spectroscopy data from Lunar Prospector. Journal of Geophysical Research, 111, E12007, doi:10.1029/2005JR002656.

Staid, M.I. and Pieters, C.M. (2001) The mineralogy of last lunar basalts: Results from Clementine. Journal of Geophysical Research, 106, 27877-27900, doi: 10.1029/2000JE001387.

Staid, M.I., et al. (2011) The mineralogy of late stage lunar volcanism as observed by the Moon Mineralogy Mapper on Chandrayaan-1. Journal of Geophysical Research, 116, E00G10, doi: 10.1029/2010JE003735.

Stöffler, D., Knoll, H.-D., Marvin, U.B., Simonds, C.H., and Warren, P.H. (1980) Recommended classification and nomenclature of lunar highland rock—A committee report. In J.J. Papike and R.B. Merrill, Eds., Proceedings of the Conference on the Lunar Highland Crust, p 51-70, Pergamon Press.

Taylor, L.A., Cahill, J.T., Patchen, A., Pieters, C., Morris, R.V., Keller, L.P., and McKay, D.S. (2001a) Mineralogical and chemical characterization of lunar high-land regolith: Lessons learned from mare soils. Lunar and Planetary Science Conference XXXII, Houston, TX, Abstract # 2196.

Taylor, L.A., Patchen, A., Cahill, J., Pieters, C.M., Morris, R.V., Keller, L.P., and Mckay, D.S. (2002) Mineral and glass characterization of Apollo 14 soils. Lunar and Planetary Science Conference XXXIII, Houston, TX, Abstract #1302.

Taylor, L.A., Patchen, A., Taylor, D.-H., Chambers, J.G., and McKay, D.S. (1996) X-ray digital imaging and petrography of lunar mare soils: Data input for remote sensing calibrations. Icarus, 124, 500-512.

Taylor, L.A., Pieters, C.M., Keller, L.P., Morris, R.V., and McKay, D.S. (2001b) Lunar mare soils: Space weathering and the major effects of surface-correlated nanophase Fe. Journal of Geophysical Research, 106, 27,985-27,999.

Taylor, L.A., Pieters, C.M., Keller, L.P., Morris, R.V., McKay, D.S., Patchen, A., and Wentworth, S. (2001c) The effects of space weathering on Apollo 17 mare soils: Petrographic and chemical characterization. Meteoritics and Planetary Science, 36, 285-299.

Taylor, L.A., Pieters, C.M., Patchen, A., Taylor, D.-H., Morris, R,V,. Keller, L.P., and McKay, D.S. (2003) Mineralogical Characterization of Lunar Highland Soils. Lunar and Planetary Science Conference XXXIV, Houston, TX, Abstract #1774.

Wieczorek, M.A., Jolliff, B.L., Khan, A., Pritchard, M.E., Weiss, B.P., Williams, J.G., Hood, L.L., Righter, K., Neal, C.R., Shearer, C.K., McCallum, I.S., Tompkins, S., Hawke, B.R., Peterson, C., Gillis, J.J., and Bussey, B. (2006) The Constitution and Structure of the Lunar Interior. In Jolliff, B.L., Wieczorek, M.A., Shearer, C.K., and Neal, C.R, Eds., New Views of the Moon, pp 221-364, Mineralogical Society of America.

Figure 1: a) Fast neutron count rate calculated from the LP GRS oxides using equation (1) plotted against measured fast neutron count rate from the LP GRS anti-coincidence shield. b) Fast neutron count rate calculated from the LP GRS oxides and equation (1) with $e = 25.6 * 10^{-3}$ and $f = 10.6$ compared with the measured fast neutron count rate. The solid black line represents where the data points would fall if the two data sets were in perfect agreement.

Figure 2: a) Measured epithermal to thermal neutron count rates from the LP NS plotted against the predicted epithermal to thermal neutron count rates as calculated using equations (2) and (3) from LP GRS oxides with Sm = 2.7 * Th (Gillis et al., 2003) and Gd = 1.17 * Sm (Jolliff, 1998; Korotev, 2000). b) Measured epithermal to thermal neutron count rates from LP NS plotted against predicted epithermal to thermal neutron count rate ratio from LP GRS calculated using equation (2) and (3) with $a = 5.732 * 10^{-3}$ and $b = 1.386 * 10^{-3}$ with Sm = 2.39 * Th and Gd = 1.17 * Sm.

Figure 3: a) FeO derived from the mineral maps of Lucey (2004) and ilmenite based on the TiO_2 abundance of Gillis et al. (2003) compared with LP GRS FeO; b) Al_2O_3; c) MgO; d) CaO; e) SiO_2; f) Spectrally-derived TiO_2 of Gillis et al. (2003), the basis for our ilmenite estimate, compared with LP GRS TiO_2. The line shown in each plot is that of a 1:1 correlation, where all points would fall if the two data sets were in perfect agreement.

Figure 4: a) Aluminum and iron oxides from the Prettyman et al. (2006) LP GRS 2 degree dataset; b) Aluminum and iron oxides calculated from the mineral maps of Lucey (2004). The solid line in each plot shows the linear relationship between aluminum and iron in lunar samples as determined by Prettyman et al. (2006): $Al_2O_3 = -1.2\ FeO + 32.4$.

Figure 5: a) White corresponds with areas of the Moon where FeO derived from the mineral maps of Lucey (2004) is less than 15 wt.% and Al_2O_3 derived from the same maps is less than 20 wt.% (areas in Fig. 4b) that fall well below the expected aluminum-iron trend from lunar samples). b) Orthopyroxene map of Lucey (2004), stretched between 5 and 10 vol.% to show a correspondence of the low-aluminum, low-iron regions shown in 5a) with higher orthopyroxene abundance.

Figure 6: Aluminum and iron oxides calculated from the optimized mineral maps. The solid line shows the linear relationship between aluminum and iron in lunar samples as determined by Prettyman et al. (2006): $Al_2O_3 = -1.2\ FeO + 32.4$.

Figure 7: a) FeO derived from the optimized mineral maps with LP GRS FeO; b) Al_2O_3; c) MgO; d) CaO; e) SiO_2; f) TiO_2. The line shown in each plot is that of a 1:1 correlation, where all points would fall if the two data sets were in perfect agreement.

Figure 8: Global maps and histograms showing Mg# for the mafic minerals from a) Lucey (2004); b) the optimized Mg# obtained by the method described in the text; c) Lunar Prospector GRS FeO and MgO maps (Prettyman et al. 2006); d) optimized Mg# from 8b with adjustments made for the Mg# of olivine in the western maria as described in this section. Black outlines show the olivine-rich western mare region adjusted in 8d.

Figure 9: FeO abundance in wt% from LP GRS compared with a) mineral-map derived FeO with lowered olivine Mg# in the western maria; b) mineral-map derived FeO with lowered olivine Mg# and increased plagioclase in the western maria. Solid lines shown in a) and b) are the line of 1:1 correlation. c) Al_2O_3 and FeO in wt% calculated from the Mg# map of Fig. 8d and the final mineral maps shown in Fig. 11. The solid line shown is the linear relationship between

aluminum and iron in lunar samples as determined by Prettyman et al. (2006): $Al_2O_3 = -1.2\ FeO + 32.4$. d) Al_2O_3 plotted against FeO + MgO for the same maps. The solid line shown is the linear trend between Al_2O_3 and FeO+MgO in lunar samples from Lucey et al. (2006): $Al_2O_3 = -0.886 * (FeO+MgO) + 36.4$.

Figure 10: Mg# maps and histograms for a) optimized Mg# obtained following the procedure described in Section 3.3.1; b) Mg# from the SELENE Spectral Profiler, obtained by Ohtake et al. (2012). Black areas were not analyzed by Ohtake et al. so are removed from both maps. Only colored regions are reflected in the histograms. General spatial agreement is seen between the two Mg# analyses.

Figure 11: Lunar major mineral global maps based on the maps of Lucey (2004) with optimization performed to bring the datasets into agreement with Lunar Prospector neutron and gamma ray results: a) plagioclase; b) clinopyroxene; c) olivine; d) orthopyroxene; e) ilmenite. The ilmenite map shown was inferred from the TiO2 map of Gillis et al. (2003), then compared with LP GRS oxides and optimized along with the mineral maps of Lucey (2004).

Figure 12: a) Mineralogy of each pixel of the lunar surface from the maps of Lucey (2004), with olivine, opx+cpx, and plagioclase re-normalized to 100% displayed with the compositional fields for highland rocks defined by Stöffler et al. (1980). The shaded field, based on Fig. 2.3 of Lucey et al. (2006), shows the compositions of lunar soils samples from the Apollo and Luna missions as well as lunar feldspathic meteorites. b) The optimized mineralogy (plagioclase-pyroxene-olivine) obtained through our comparison to Lunar Prospector shows greatly improved agreement with known soils. c) Optimized mineralogy from this study plotted on a plagioclase-orthopyroxene-clinopyroxene ternary displayed on the compositional fields

493 defined by Stöffler et al. (1980). The shaded field covers the mineralogy distribution of lunar
494 soil samples measured by the Lunar Soils Characterization Consortium (Taylor et al., 1996,
495 2001a,b,c, 2002, 2003; Pieters et al. 2002).

496

Table 1: Thermal neutron absorption cross sections for the major lunar elements and Sm and Gd
Note: [a]The neutron absorption cross sections for isotopes of Sm and Gd vary widely. The values given are the neutron absorption cross sections of the most highly absorbing isotopes; absorption for other isotopes are generally below 1 (NNDC, accessed Dec. 2010).

Element	Thermal neutron absorption cross section (barns)
O	0.00019
Na	0.528
Mg	0.063
Al	0.233
Si	0.16
Ca	0.43
Ti	6.11
Fe	2.59
Sm[a]	56000
Gd[a]	90000

Table 2. Comparison of literature values for the constants in equations 1 and 2 for comparing neutron flux with gamma ray elemental abundances with the modified values obtained in this work to bring the two datasets into agreement.

	Parameter	Literature values	This work
Fast neutron and gamma ray reconciliation	e	$26 +/- 6 * 10^{-3}$ (Gasnault et al., 2001)	$25.6 * 10^{-3}$
	f	11 +/- 3 (Gasnault et al., 2001)	10.6
Thermal and epithermal neutron and gamma ray reconiciliation	a	$5.252 * 10^{-3}$ (Elphic et al., 2000)	$5.732 * 10^{-3}$
	b	$1.485 * 10^{-3}$ (Elphic et al., 2000)	$1.386 * 10^{-3}$
	Sm/Th	2.7 (Gillis et al. 2003)	2.39

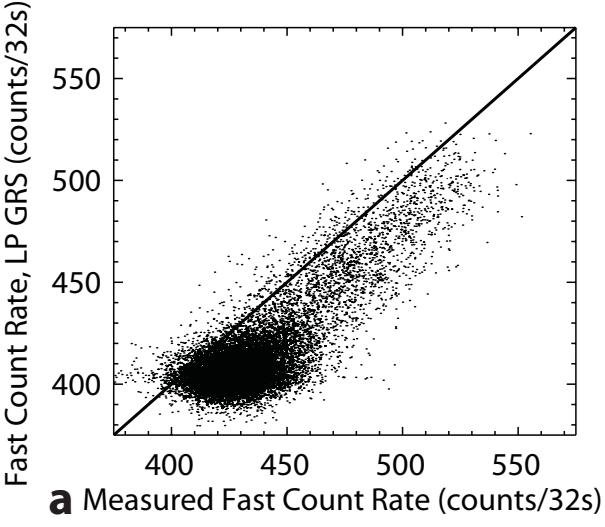
Fast Count Rate, LP GRS (counts/32s)
550
500
450
400
400
450
500
550
a Measured Fast Count Rate (counts/32s)

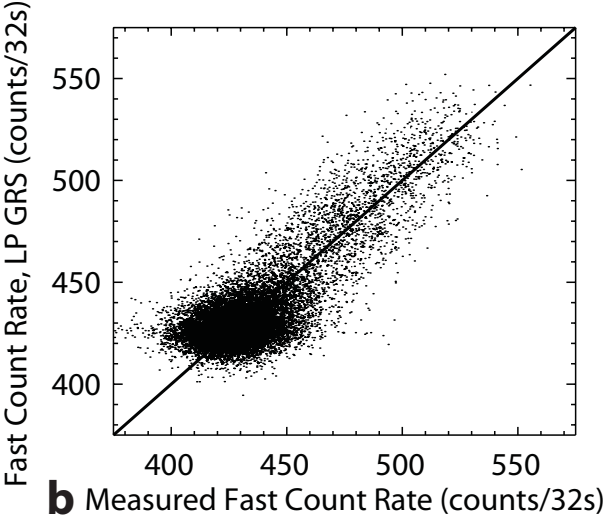
Fast Count Rate, LP GRS (counts/32s)
550
500
450
400
400
450
500
550
b Measured Fast Count Rate (counts/32s)

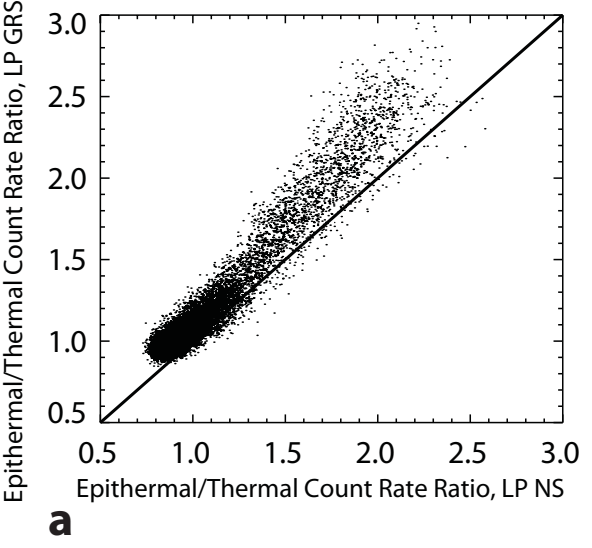
Epithermal/Thermal Count Rate Ratio, LP GRS
3.0
2.5
2.0
1.5
1.0
0.5
0.5
1.0
1.5
2.0
2.5
3.0
Epithermal/Thermal Count Rate Ratio, LP NS
a

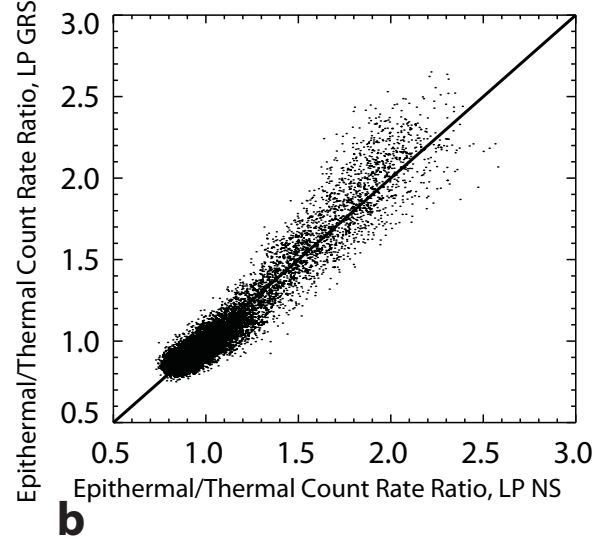
Epithermal/Thermal Count Rate Ratio, LP GRS
3.0
2.5
2.0
1.5
1.0
0.5
0.5
1.0
1.5
2.0
2.5
3.0
Epithermal/Thermal Count Rate Ratio, LP NS
b

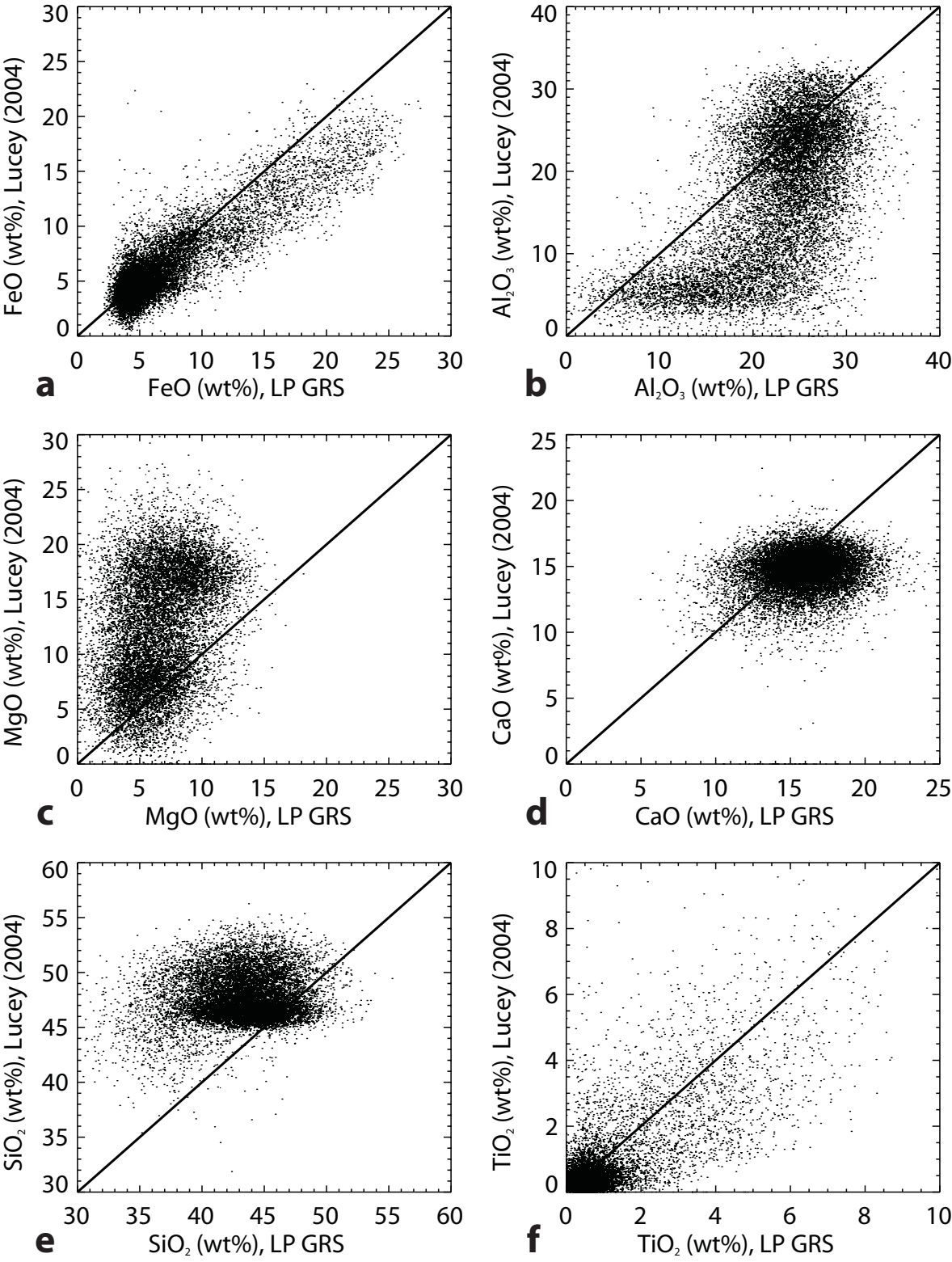
FeO (wt%), Lucey (2004)
FeO (wt%), LP GRS
a
Al_2O_3 (wt%), Lucey (2004)
Al_2O_3 (wt%), LP GRS
b
MgO (wt%), Lucey (2004)
MgO (wt%), LP GRS
c
CaO (wt%), Lucey (2004)
CaO (wt%), LP GRS
d
SiO_2 (wt%), Lucey (2004)
SiO_2 (wt%), LP GRS
e
TiO_2 (wt%), Lucey (2004)
TiO_2 (wt%), LP GRS
f

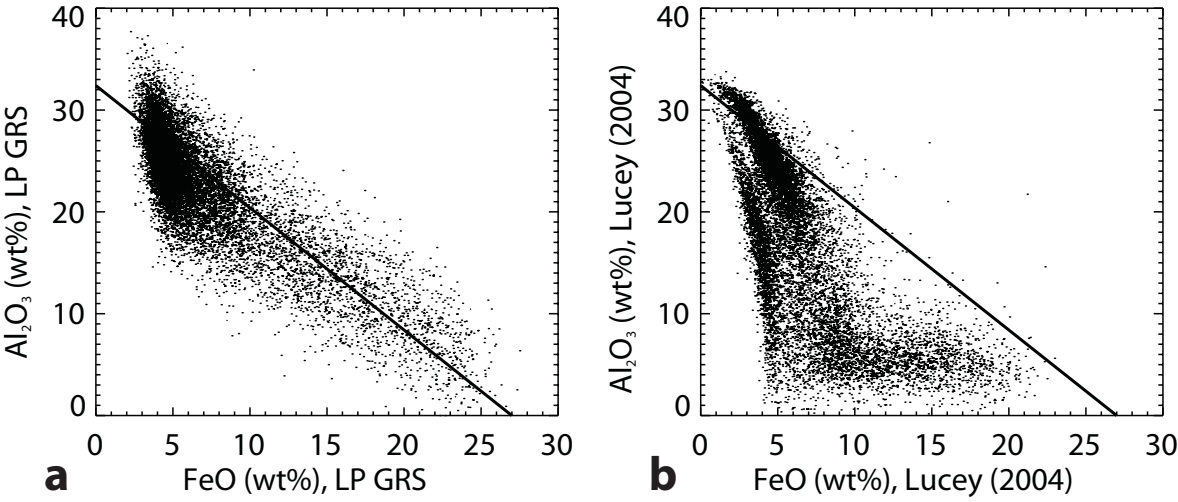
40
30
20
10
0
0
5
10
15
20
25
30
Al2O3 (wt%), LP GRS
FeO (wt%), LP GRS
a
Al2O3 (wt%), Lucey (2004)
FeO (wt%), Lucey (2004)
b

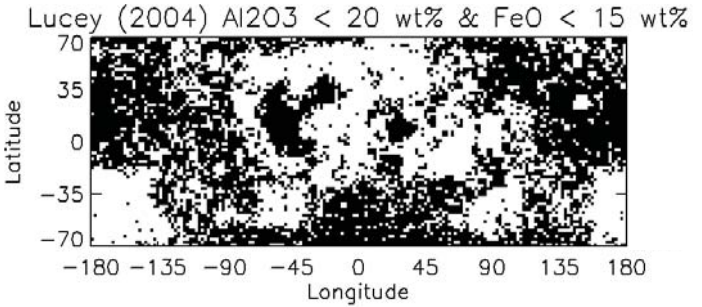
Lucey (2004) Al2O3 < 20 wt% & FeO < 15 wt%
Latitude
70
35
0
−35
−70
−180 −135 −90 −45 0 45 90 135 180
Longitude

a

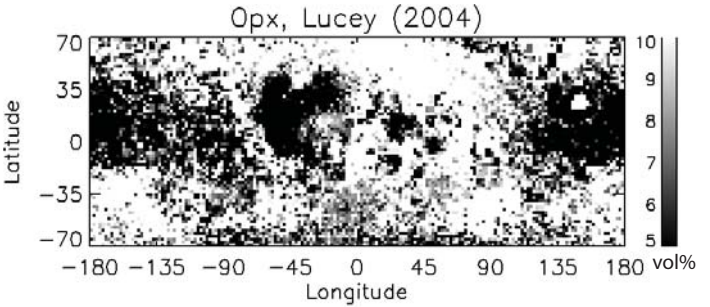
Opx, Lucey (2004)
Latitude
70
35
0
−35
−70
−180 −135 −90 −45 0 45 90 135 180
Longitude
10
9
8
7
6
5
vol%

b

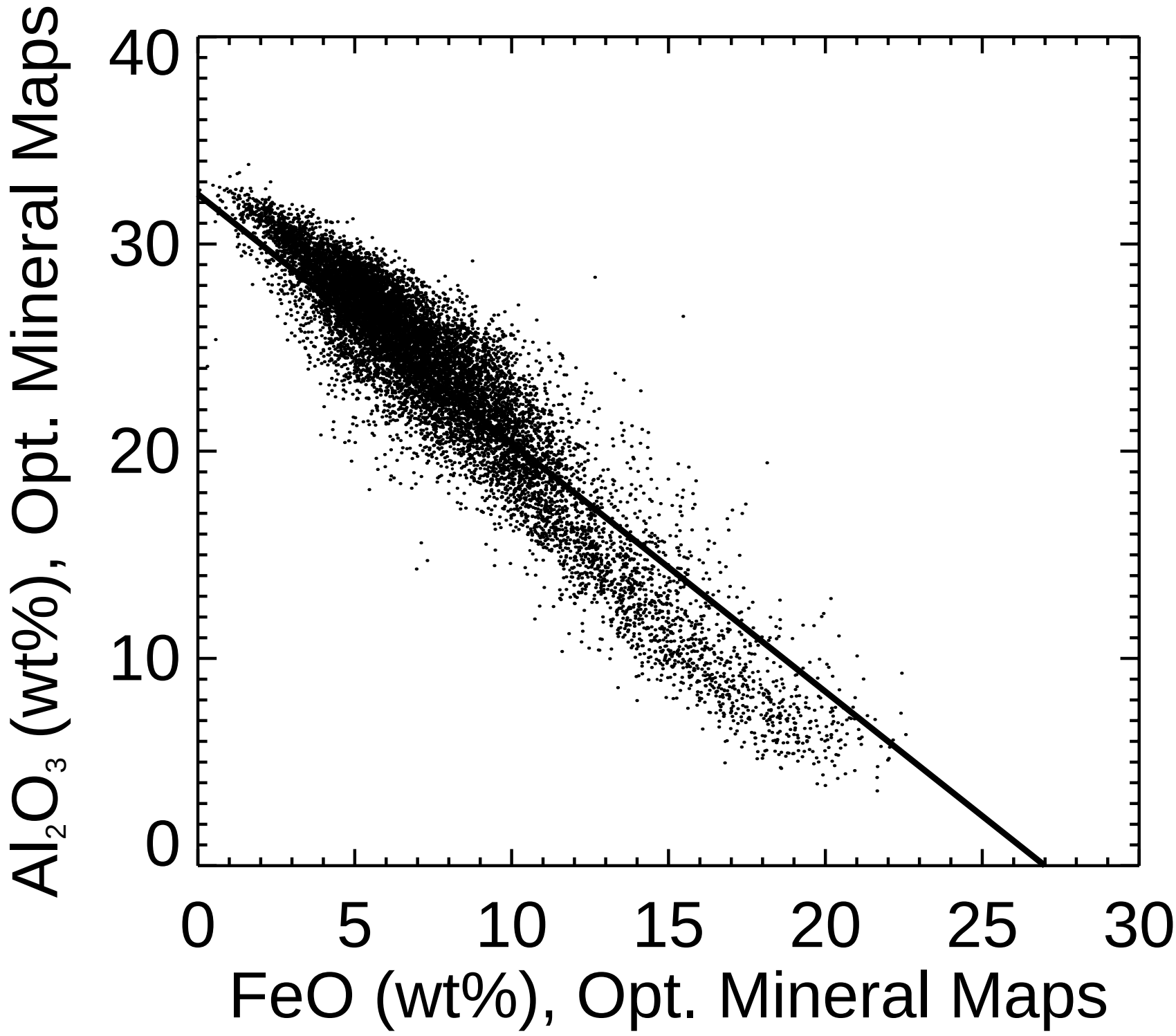
40
30
20
10
0
Al_2O_3 (wt%), Opt. Mineral Maps
0
5
10
15
20
25
30
FeO (wt%), Opt. Mineral Maps

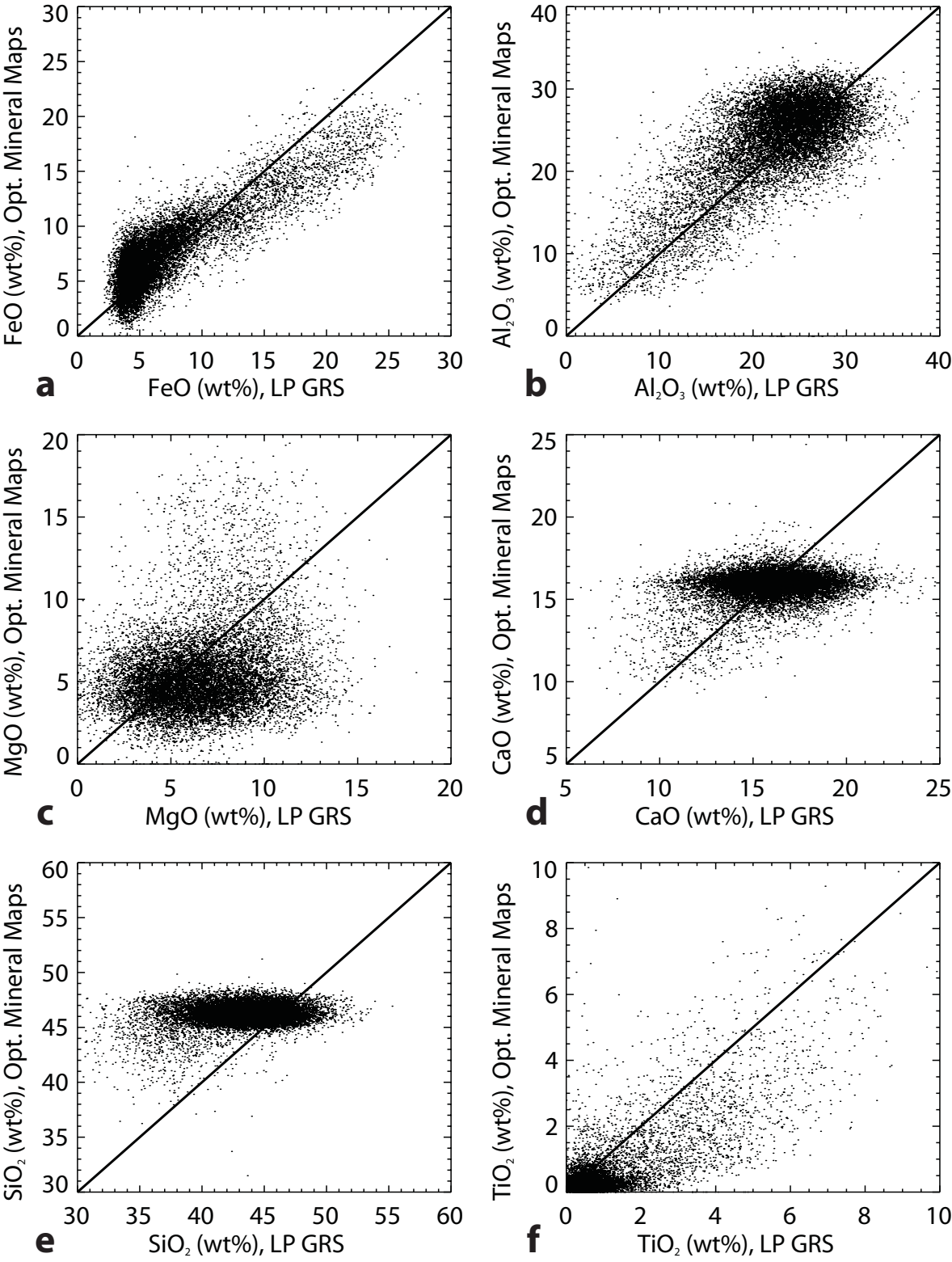
FeO (wt%), Opt. Mineral Maps
FeO (wt%), LP GRS
a
Al_2O_3 (wt%), Opt. Mineral Maps
Al_2O_3 (wt%), LP GRS
b
MgO (wt%), Opt. Mineral Maps
MgO (wt%), LP GRS
c
CaO (wt%), Opt. Mineral Maps
CaO (wt%), LP GRS
d
SiO_2 (wt%), Opt. Mineral Maps
SiO_2 (wt%), LP GRS
e
TiO_2 (wt%), Opt. Mineral Maps
TiO_2 (wt%), LP GRS
f

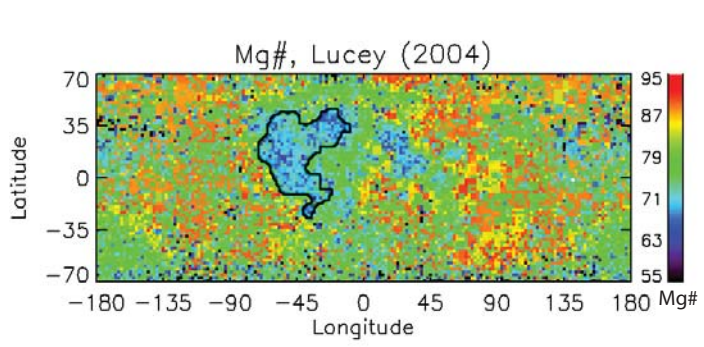
Mg#, Lucey (2004)
Latitude
Longitude
Mg#

a

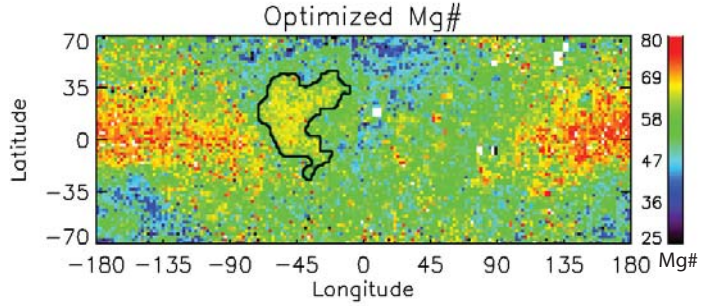
Optimized Mg#
Latitude
Longitude
Mg#

b

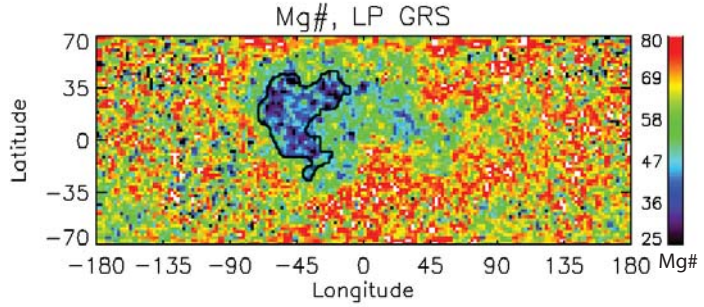
Mg#, LP GRS
Latitude
Longitude
Mg#

c

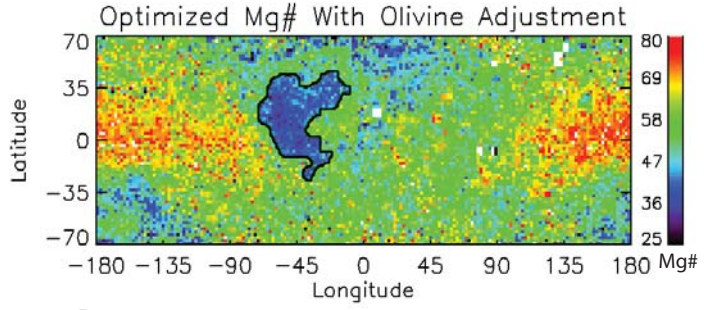
Optimized Mg# With Olivine Adjustment
Latitude
Longitude
Mg#

d

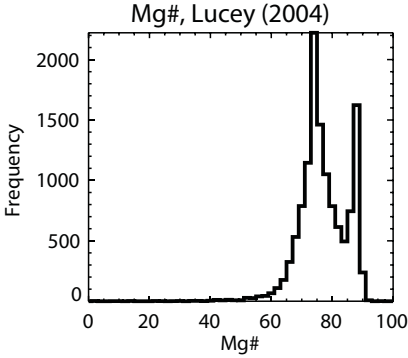
Mg#, Lucey (2004)
Frequency
Mg#

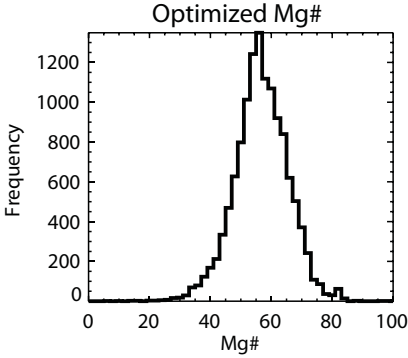
Optimized Mg#
Frequency
Mg#

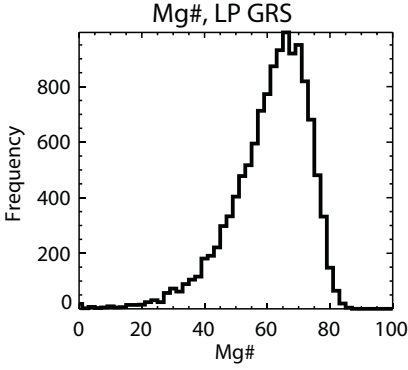
Mg#, LP GRS
Frequency
Mg#

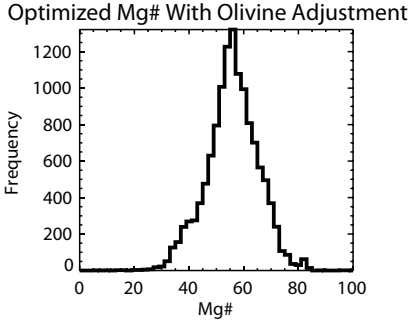
Optimized Mg# With Olivine Adjustment
Frequency
Mg#

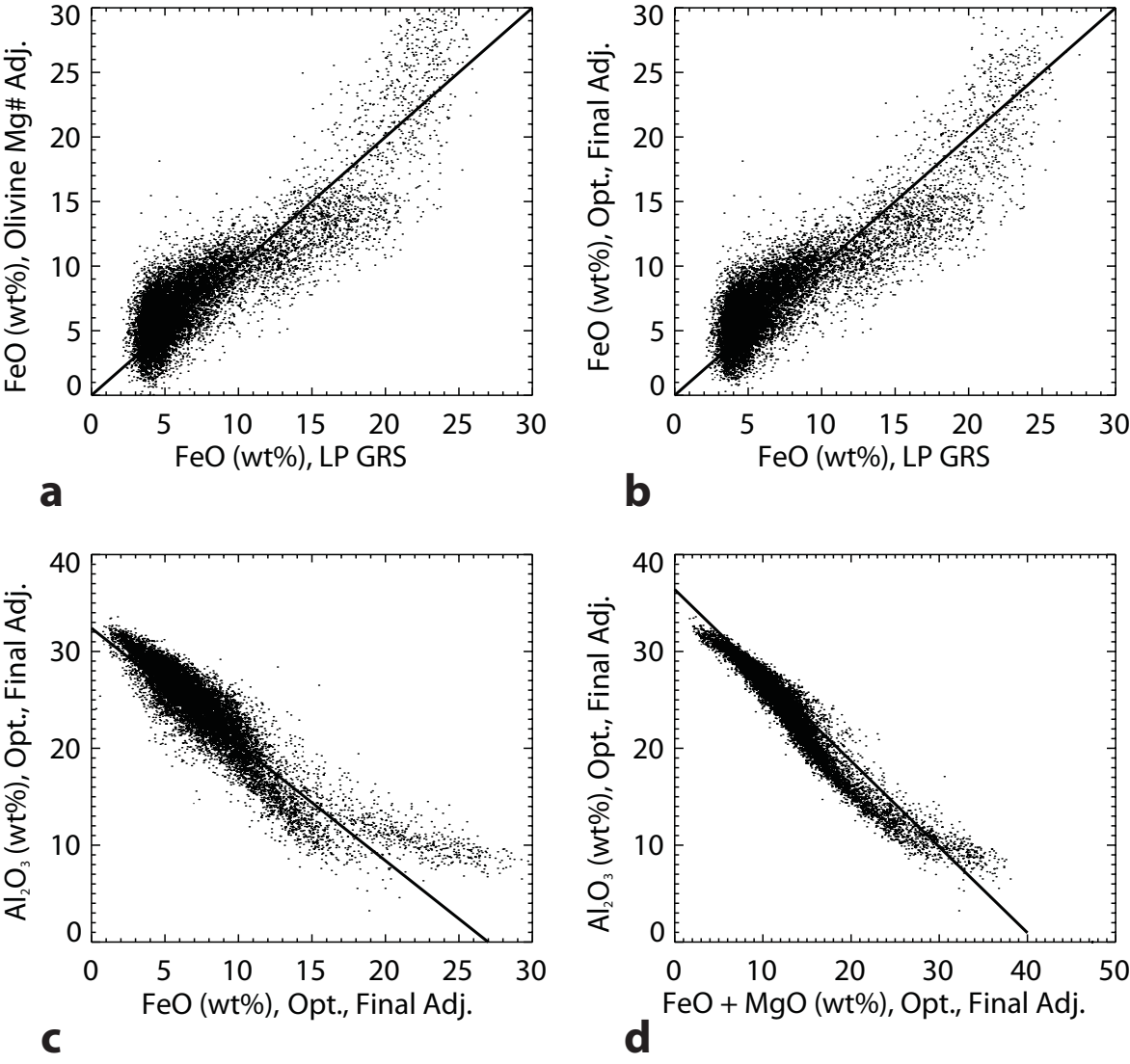
FeO (wt%), Olivine Mg# Adj.
FeO (wt%), LP GRS
a
FeO (wt%), Opt., Final Adj.
FeO (wt%), LP GRS
b
Al2O3 (wt%), Opt., Final Adj.
FeO (wt%), Opt., Final Adj.
c
Al2O3 (wt%), Opt., Final Adj.
FeO + MgO (wt%), Opt., Final Adj.
d

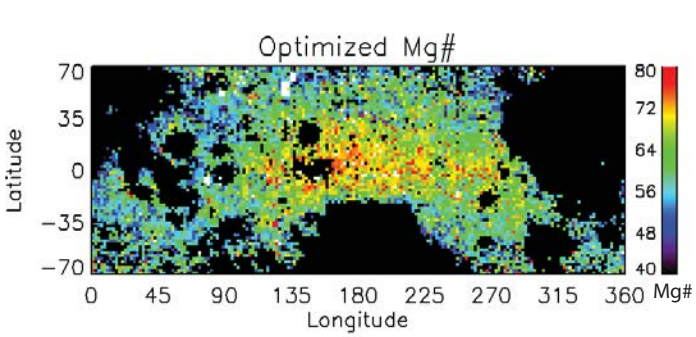
Optimized Mg#
Latitude
70
35
0
−35
−70
0 45 90 135 180 225 270 315 360
Longitude
80
72
64
56
48
40
Mg#

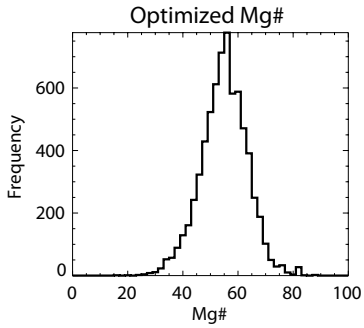
Optimized Mg#
Frequency
600
400
200
0
0 20 40 60 80 100
Mg#

a

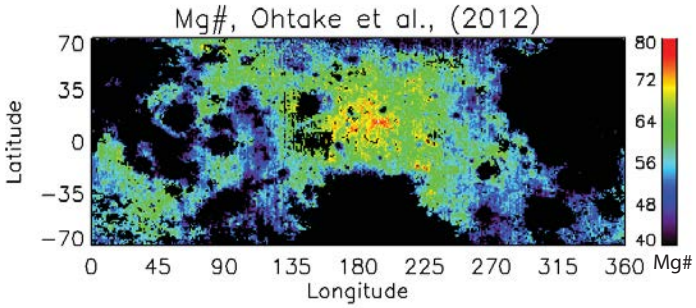
Mg#, Ohtake et al., (2012)
Latitude
70
35
0
−35
−70
0 45 90 135 180 225 270 315 360
Longitude
80
72
64
56
48
40
Mg#

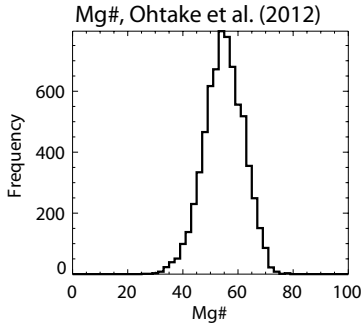
Mg#, Ohtake et al. (2012)
Frequency
600
400
200
0
0 20 40 60 80 100
Mg#

b

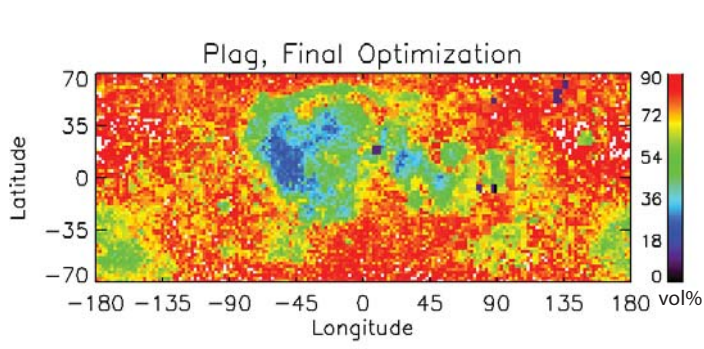
Plag, Final Optimization
Latitude
Longitude
vol%

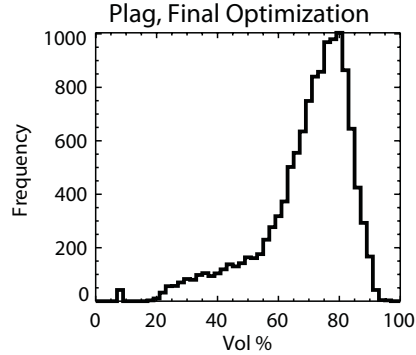
Plag, Final Optimization
Frequency
Vol %

a

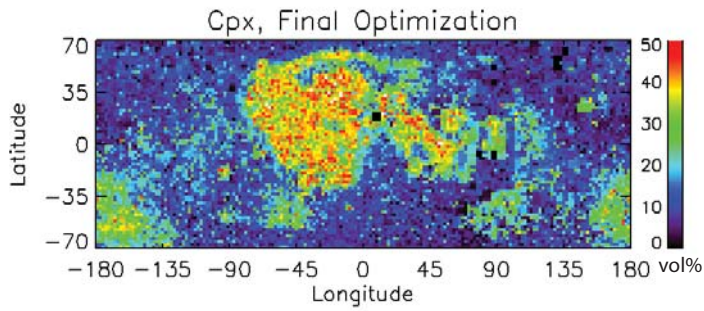
Cpx, Final Optimization
Latitude
Longitude
vol%

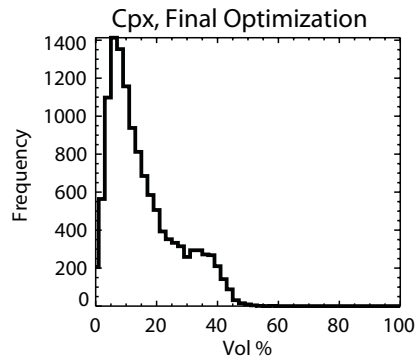
Cpx, Final Optimization
Frequency
Vol %

b

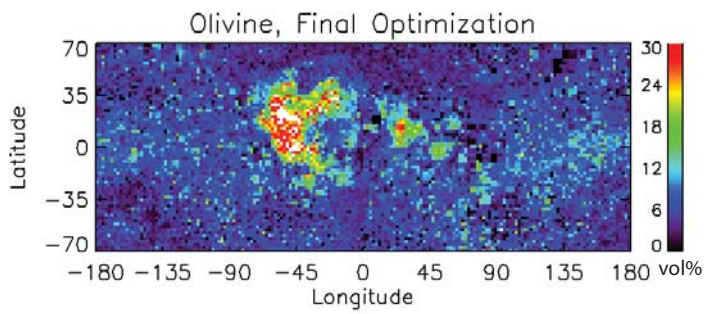
Olivine, Final Optimization
Latitude
Longitude
vol%

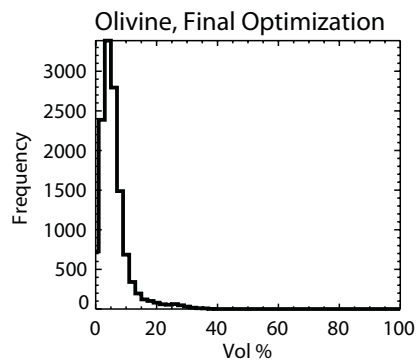
Olivine, Final Optimization
Frequency
Vol %

c

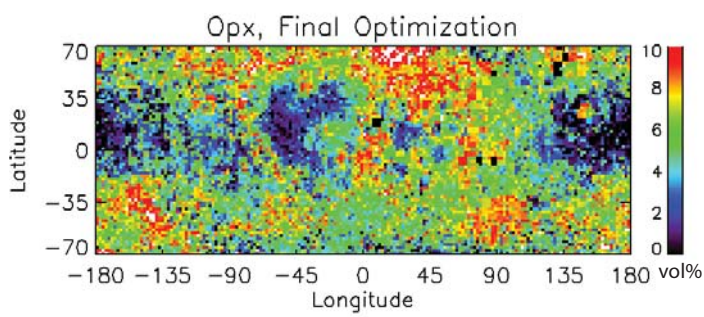
Opx, Final Optimization
Latitude
Longitude
vol%

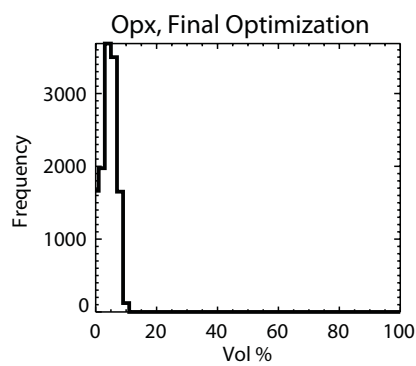
Opx, Final Optimization
Frequency
Vol %

d

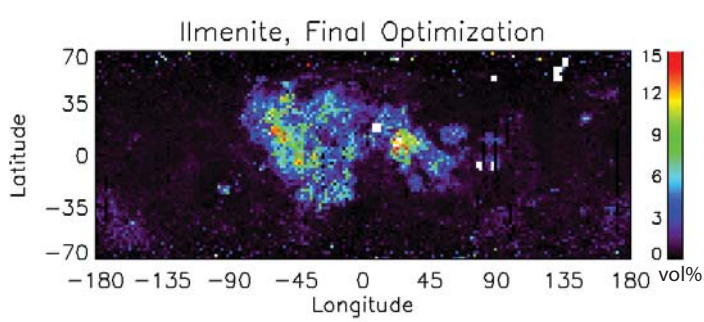
Ilmenite, Final Optimization
Latitude
Longitude
vol%

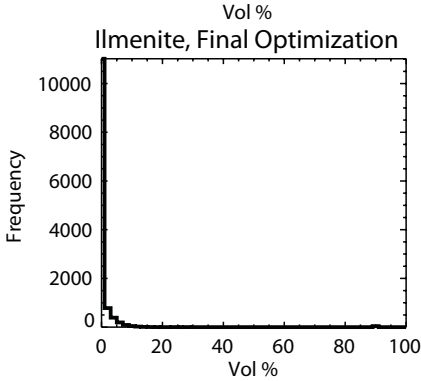
Ilmenite, Final Optimization
Frequency
Vol %

e

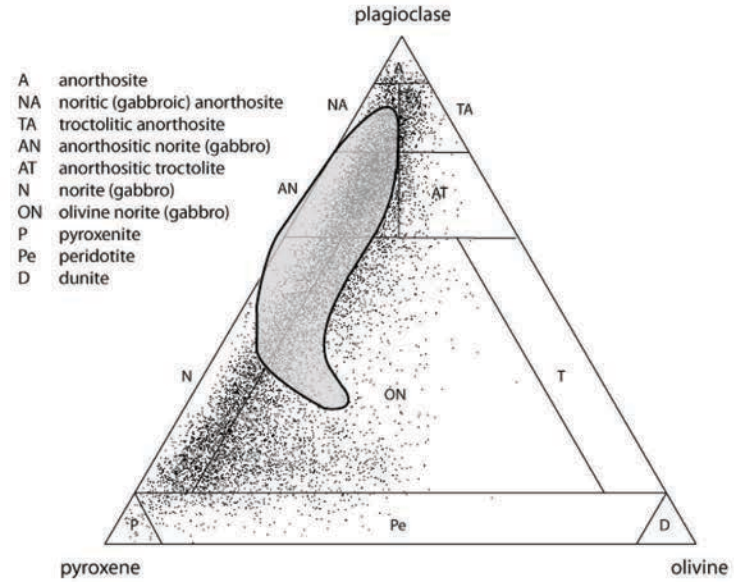
plagioclase
A anorthosite
NA noritic (gabbroic) anorthosite
TA troctolitic anorthosite
AN anorthositic norite (gabbro)
AT anorthositic troctolite
N norite (gabbro)
ON olivine norite (gabbro)
P pyroxenite
Pe peridotite
D dunite
A
NA
TA
AN
AT
N
ON
T
P
Pe
D
pyroxene
olivine

a

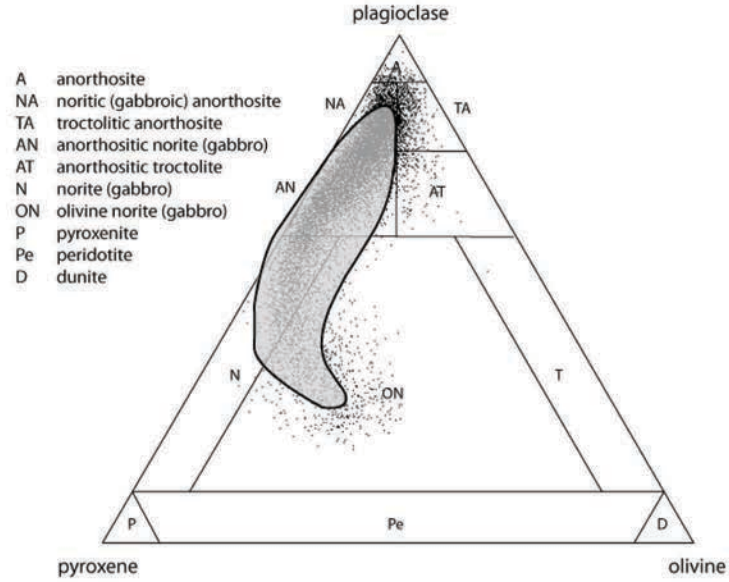
plagioclase
A anorthosite
NA noritic (gabbroic) anorthosite
TA troctolitic anorthosite
AN anorthositic norite (gabbro)
AT anorthositic troctolite
N norite (gabbro)
ON olivine norite (gabbro)
P pyroxenite
Pe peridotite
D dunite
A
NA
TA
AN
AT
N
ON
T
P
Pe
D
pyroxene
olivine

b

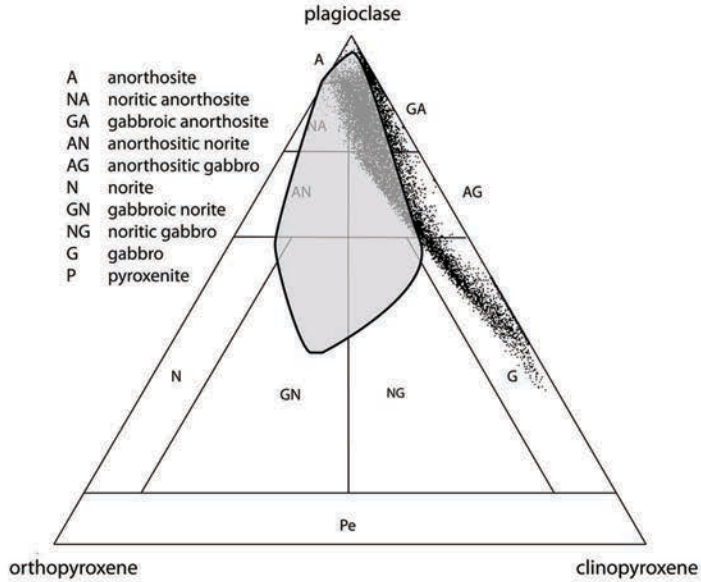
plagioclase
A anorthosite
NA noritic anorthosite
GA gabbroic anorthosite
AN anorthositic norite
AG anorthositic gabbro
N norite
GN gabbroic norite
NG noritic gabbro
G gabbro
P pyroxenite
A
NA
GA
AN
AG
N
GN
NG
G
Pe
orthopyroxene
clinopyroxene

c